Applied Surface Science 459 (2018) 453–458

Contents lists available at ScienceDirect

Applied Surface Science

journal homepage: www.elsevier.com/locate/apsusc

Full Length Article

N-doped hollow carbon nanospheres as platinum anchoring material for efficient hydrogen evolution

Lili Fan[a], Xinxin Du[a], Zixi Kang[a], Hailing Guo[b], Wenpei Kang[a], Ming Xue[c,*], Daofeng Sun[a,*]

[a] College of Science, China University of Petroleum (East China), Qingdao, Shandong 266580, PR China
[b] State Key Laboratory of Heavy Oil Processing, Key Laboratory of Catalysis, China National Petroleum Corp. (CNPC), China University of Petroleum (East China), Qingdao 266555, PR China
[c] State Key Laboratory of Inorganic Synthesis and Preparative Chemistry, Jilin University, 130012 Changchun, PR China

ARTICLE INFO

Keywords:
Hydrogen evolution
Electrocatalyst
Platinum anchoring
Metal-organic frameworks
Carbon nanosphere

ABSTRACT

Platinum-based materials remain as the most effective electrocatalysts for hydrogen evolution reaction. Smarter material and strategy for anchoring platinum with enhanced utilization efficiency are highly demanded. In this work, N-doped hollow carbon nanospheres are prepared targetedly from a metal-organic framework for *in-situ* platinum dispersion. Through a simple electrochemical method, platinum nanoparticles are successfully anchored on the surface of the carbon nanospheres decorated electrode, which exhibits exceptional HER performance in H_2SO_4 with low onset overpotential, small Tafel slope (33 mV decade^{-1}), high current density (overpotentials of 40 mV to reach the current density of 10 mA cm^{-2}) and high stability (4000 cyclic voltammetry (CV) cycles and total 30 h of high current density (10, 50 and 100 mA cm^{-2}) chronoamperometric electrolysis). The superior electrocatalytic activity and durability can be attributed to the facilitated electron transport and synergistic effects between platinum and carbon nanospheres. This work provides an insight into the development of efficient support materials from MOFs to design efficient platinum-based electrocatalysts for future water splitting.

1. Introduction

Hydrogen, as the cleanest energy source, has been considered to represent one of the most promising alternatives for traditional fossil fuels when facing the energy crisis, which inspires great enthusiasm for pursuing technologies of sustainable hydrogen production [1–4]. Electrochemical water splitting, which includes the hydrogen evolution as half reaction, has been considered as an alternative for efficient hydrogen production [5,6]. Electrocatalysts are extremely desirable for hydrogen evolution reaction (HER) for overcoming the inherent thermodynamic overpotential and increasing the energy conversion efficiency [7]. Although numerous noble-metal-free electrocatalysts have been developed in strong acids, including the transition metal compounds (sulfides, [8,9] oxides, [10] nitrides, [11] carbides, [12] borides, [13] and phosphides [14–16]) and carbon-based materials, [17–19] platinum (Pt)-based materials remain the most effective electrocatalysts for HER due to its extreme chemical inertness and near-zero overpotential [20,21]. Unfortunately, the elemental scarcity and high cost of Pt, in addition to the vulnerability to aggregation and subsequently drastic reduction in catalytic performance, greatly impedes its commercial application as a HER catalyst. Thus, smarter material and strategy for fabricating Pt-based electrocatalysts with enhanced utilization efficiency and prolonged stability and durability are highly demanded.

Carbon materials with graphitic structures (such as graphene, carbon nanotubes) have been widely explored as conductive support materials for heterogeneous catalysts [22,23]. They are reported to generally boost the catalytic performances of the supported catalysts, which could be caused by their large surface area, excellent electronic conductivity and good stability [24–26]. In addition, heteroatom dopants of carbon materials, such as nitrogen (N), could introduce chemically active sites and also act as anchoring sites for the deposition and stabilization of metal species [27]. Hence, doping with N atoms is beneficial to improve the metal-support interaction. This makes N-doped graphitic carbons an ideal candidate for dispersing Pt group metal [42]. Regardless, rational design of new N-enriched graphitic nanocarbon supports is still necessary for the development of efficient HER catalysts.

Metal–organic frameworks (MOFs), as a new type of porous materials with modularly tuneable structures and versatile functionalities,

* Corresponding authors.
E-mail addresses: xueming@jlu.edu.cn (M. Xue), dfsun@upc.edu.cn (D. Sun).

https://doi.org/10.1016/j.apsusc.2018.08.033
Received 12 June 2018; Received in revised form 30 July 2018; Accepted 3 August 2018
Available online 04 August 2018
0169-4332/

[28–32] have recently attracted tremendous attention as self-sacrificial precursors to derive promising carbon-based materials, [33–40] which possess high surface area and exhibit good performance in gas storage, [41] supercapacitors, [42] water splitting, [43] rechargeable batteries, [44–47] and catalysis, [48–50], etc. The organic ligands in MOFs structures act as carbon sources during pyrolysis, and N atoms can be *in-situ* doped into the final product uniformly by selecting N-rich ligands with imidazoles, pyridyl or amino groups, etc. Meanwhile, various metal centers (such as Ni, Co) have a positive impact on promoting the graphitization degree of the carbon matrix, enhancing electronic properties and durability of the material. Regulation of synergism of organic ligands and metal centers can be realized by choosing precise MOF structure.

So far, several approaches have been adopted to disperse noble metal nanoparticals (NPs) either on the surface or inside the carbon support [51,52]. In general, metal sources are firstly blended with carbon/carbon precursor, then followed by a reduction or thermal treatment process. For practical use, smarter methods that can deposit the noble metal NPs more accurately, simplify the preparation steps, or minimize the consumption of metal source are in demand. The recently proposed anodic dissolution of Pt counter electrode during HER process and following reduction of Pt on the working electrode can be utilized as an effective strategy to disperse Pt NPs for preparing high performance Pt-based HER catalyst. Though a few attempts have been made in this respect, substantial studies are still demanded contributing to the design and synthesis of advanced materials for Pt NPs anchoring.

Herein, we present the N-doped hollow carbon nanospheres (denoted as N-HCNs) as anchoring material for Pt deposition to prepare efficient HER catalyst. A N-rich MOF, Ni_2(L-asp)$_2$(pz) (known as JUC-150, [53] L-asp = L-aspartic acid, pz = pyrazine) was selected as the "proof of concept" precursor to prepare N-HCNs due to its special features. The final graphitization degree of the carbon matrix can be promoted by the Ni centers, most of which, however, would escape from the encapsulation of carbon matrix. The readily available amino acid as well as pyrazine N-rich ligands can afford *in-situ* N-doped carbon structures without any additional nitrogen source. These N atoms are doped as Pt anchoring sites during the electrochemical deposition process of subjecting the N-HCNs decorated electrode to cathodic multicyclic voltammetry (CV) scans. The total numbers of CV cycles effect the final catalytic performance. After 8000 CV cycles, exceptional HER performance of low onset overpotential, small Tafel slope, high current density and superior stability was obtained. The excellent electrocatalytic activity and durability can be attributed to the facilitated electron transport and synergistic effects between Pt and N-HCNs, which provides an insight into the development of efficient support materials for Pt deposition.

2. Experimental section

2.1. Chemicals

All chemicals were purchased and used without further purification. Nickel (II) carbonate basic hydrate (48–50% Ni, Fluka), L-aspartic acid (98%, Sigma-Aldrich), pyrazine (99%, Sigma-Aldrich), Pt/C (5% on carbon, Alfa Aesar), Nafion-117 solution (5% in a mixture of lower aliphatic alcohols and water) (Sigma-Aldrich), sulphuric acid (98%, Merck) and hydrochloric acid (32%, RCI labscan) were used as received.

2.2. Synthesis of Ni(L-asp)(H_2O)$_2$·H_2O

Measured amount of $NiCO_3$·2Ni$(OH)_2$·xH_2O (2.450 g) and L-aspartic acid (2.630 g) were dissolved in water (200 mL) while stirred and heated for 3 h. After all the remaining solid particles were filtered out, the clear turquoise solution was then evaporated at 80 °C oven overnight to obtain the pale blue Ni(L-asp)(H_2O)$_2$·H_2O powder.

2.3. Synthesis of JUC-150

Ni(L-asp)(H_2O)$_2$·H_2O (0.219 g) and pyrazine (0.156 g) were dispersed in a mixture containing water (6 mL) and methanol (6 mL) under ultrasonic vibration. The final solution was sealed into an autoclave and heated at 150 °C for 48 h. The product was filtered, washed with copious amounts of water then methanol and dried at 60 °C for 24 h.

2.4. Preparation of N-HCNs

Carbonization processes were carried out in N_2 atmosphere. The dried JUC-150 powder was pretreated at 150 °C for 2 h and then maintained at 600 °C for 5 h with a heating rate of 5 °C min^{-1}. The sample obtained was further washed with concentrated HCl to remove the accessible Ni species. Then, the black powder was washed with water and dried at 60 °C for 24 h.

2.5. Characterization

Powder X-ray diffraction (XRD) patterns were acquired at room temperature using a XPert Pro MPD diffractometer with Cu Kα radiation (λ = 1.5418 Å). Transmission electron microscopy (TEM) images were collected on a Tecnai-G20 with an acceleration voltage of 200 kV. Thermogravimetric analyses were performed using a STA 449 F3 Jupiter thermal analyzer at a heating rate of 5 °C min^{-1} from 50 °C to 750 °C in argon atmosphere. Raman spectrum was recorded on a DXR Raman Microscope spectrometer with the excitation wavelength of 532 nm. X-ray photoelectron spectrum (XPS) data was carried out on an ESCALAB 250Xi Spectrometer and the binding energies were calibrated based on the graphite C 1s peak. Inductively coupled plasma-mass spectrometry (ICP-MS) results were collected via an Optima 8000 spectrometer.

2.6. Electrochemical measurements

All electrochemical measurements were performed on a Gamry electrochemical work station (INTERFACE 1000 T) with a rotating electrode system (RDE710 Rotating Electrode) at room temperature. A three-electrode cell configuration was employed by using a glassy carbon rotating disk (RED, 5.0 mm in diameter) as the working electrode, a platinum plate electrode as the counter electrode and a saturated calomel electrode (SCE) as the reference electrode. All potentials were referenced to the reversible hydrogen electrode (RHE) calibrated by adding a value of 0.253 V in 0.5 M H_2SO_4. The catalyst inks were prepared by dispersing 4 mg of sample and 80 μL of 5 wt% Nafion solution in 1 mL solution of water/ethanol (4:1, v/v) by 1 h sonication. Then 15 μL of the catalyst ink was pipetted onto the pre-cleaned glassy carbon electrode with a loading equivalent to 0.283 mg cm^{-2}. The linear sweep voltammograms (LSVs) were collected at a scan rate of 5 mV s^{-1}. Pt deposition was carried out through cyclic voltammetric sweeps at 100 mV s^{-1} between +0.905 V and −0.095 V for 8000 cycles. AC impedance measurements were carried out when the working electrode was biased at −22 mV vs. RHE from 10^5 Hz to 10^{-2} Hz with an AC voltage of 5 mV. Chronoamperometric measurements were performed at overpotential of 30, 87 and 147 mV respectively to evaluate the long-term stability.

3. Results and discussion

The JUC-150 MOF used as precursor in this work presents a layer-pillared 3D structure generated by pz ligand acting as a pillar to support the adjacent Ni(L-asp) layers, which can be stable to 400 °C (Fig. S1a). The synthesized JUC-150 powder exhibits good crystallinity that is consistent well with the simulated powder X-ray diffraction (PXRD) pattern (Fig. S1b). The pyrolysis of JUC-150 was carried out at 600 °C in nitrogen atmosphere, followed by washing with HCl and water

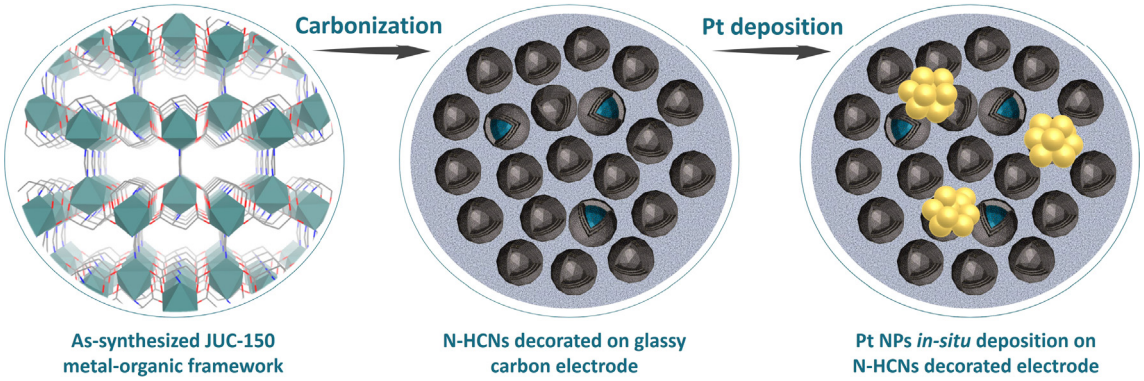

Fig. 1. Schematic illustration of the fabrication procedures for N-HCNs and *in-situ* Pt deposition on N-HCNs decorated electrode.

respectively to give N-HCNs material. The N-HCNs were decorated on glassy carbon electrode, which was subsequently subjected to cathodic multicyclic voltammetry (CV) scans for *in-situ* deposition of Pt NPs (Fig. 1). With the increase of potential cycles, the HER performance improved significantly until it reached a stable state after 8000 cycles. The sample after this process was denoted as Pt@N-HCNs.

Supplementary data associated with this article can be found, in the online version, at https://doi.org/10.1016/j.apsusc.2018.08.033.

Transmission electron microscopy (TEM) images of N-HCNs (Fig. 2) clearly show that the carbon spheres derived from MOF JUC-150 possesses a relatively narrow size distribution (in the range of 8–15 nm, Fig. S2a) with an average diameter around 10.3 nm. The lattice fringes of about 0.36 nm agrees well with the (0 0 4) planes of carbon. The residual Ni centers show lattice fringes spacing of 0.21 nm consistent with the (1 1 1) planes of nickel (Fig. S2b). The N-HCNs comes from the carbonization of organic ligands and are partially graphitized due to the catalytic graphitization behavior of nickel, which is further confirmed by the Raman spectrum (Fig. 3b). The nanosized and partially graphitized structure of N-HCNs is beneficial to electrochemical process by providing good conductivity that can facilitate the electron transport.

The structure information of N-HCNs was also collected by PXRD measurement (Fig. 3a). As shown, a broad shoulder peak is observed in the range of 20–30° (2θ), which can be attributed to the partially graphitized carbon structure (JSPDS No. 26-1080). The diffraction peaks appearing at 44.5°, 51.9° and 76.6° belong to the residual Ni centers (JSPDS NO. 04-0850). Elemental composition of N-HCNs was further investigated by X-ray photoelectron spectroscopy (XPS), which reveals the presence of C, N, Ni and O (Figs. 3c, d and S2c and d). Corresponding elemental concentration in N-HCNs is provided in Table S1. The high-resolution C 1s spectrum (Fig. 3c) can be deconvolved into four bands, corresponding to C—C at 284.6 eV, C═N at 285.9 eV, C═O at 287.6 eV and O═C—O at 290.8 eV, respectively. In the N 1s spectrum, three different N species are identified (Fig. 3d) associated with pyridinic-N (398.5 eV), pyrrolic-N (399.3 eV) and graphitic-N (401.5 eV), respectively. These N atoms are confirmed to be uniformly doped in N-HCNs (Fig. 4d), which account for active sites for Pt deposition and hydrogen evolution.

Pt NPs were *in-situ* deposited on the surface of N-HCNs decorated electrodes by a simple electrochemical approach, which was carried out by 8000 CV cycles between +0.905 V and −0.095 V. Fig. 4 shows the corresponding TEM images of the Pt@N-HCNs material collected by ultrasonic vibration from the electrode surface. The deposited Pt NPs are observed to be uniform-sized of about 8 nm (Fig. 4b). The HRTEM image offers its lattice fringes with an interplanar distance of around 0.22 nm, matching well with the (1 1 1) planes of the cubic Pt phase. The selected area elec-tron electron diffraction pattern exhibits concentric rings consisting of discrete diffraction dots that can be assigned to Pt (1 1 1), Ni (1 1 1) and Pt (3 1 1), respectively. To demonstrate the distribution of elements, elemental mappings were recorded (Fig. 4d). As can be seen, the C, Ni and N are homogeneously distributed, while the agminated Pt further indicates that Pt NPs are post-deposited, which is originated in dissolution of the counter electrode during the CV cycles followed by reduction at the surface of working electrode. The existence of Pt was also certified by XPS spectrum (Fig. 5e). Two Pt 4f peaks located at 74.1 and 70.8 eV correspond to the binding energies of Pt $4f_{7/2}$ and Pt $4f_{5/2}$, respectively. We can further deconvolute the Pt 4f XPS spectrum into metallic Pt and oxidized Pt, which originates from the natively passivated PtO layer [20]. From the result of inductively coupled plasma-mass spectrometry (ICP-MS), the content of platinum in Pt@N-HCNs was confirmed to be around 7.5 wt%, indicating that the

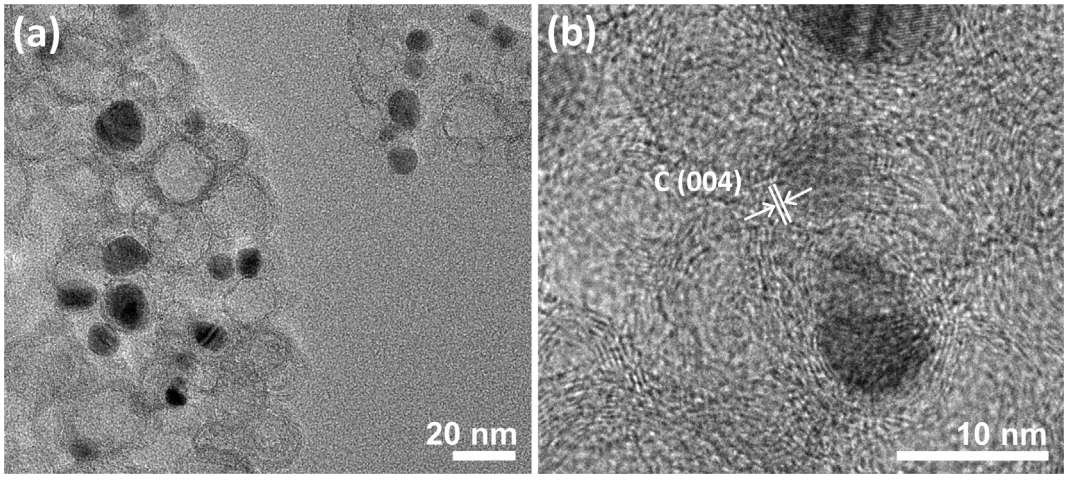

Fig. 2. (a) TEM image and (b) HRTEM image of N-HCNs.

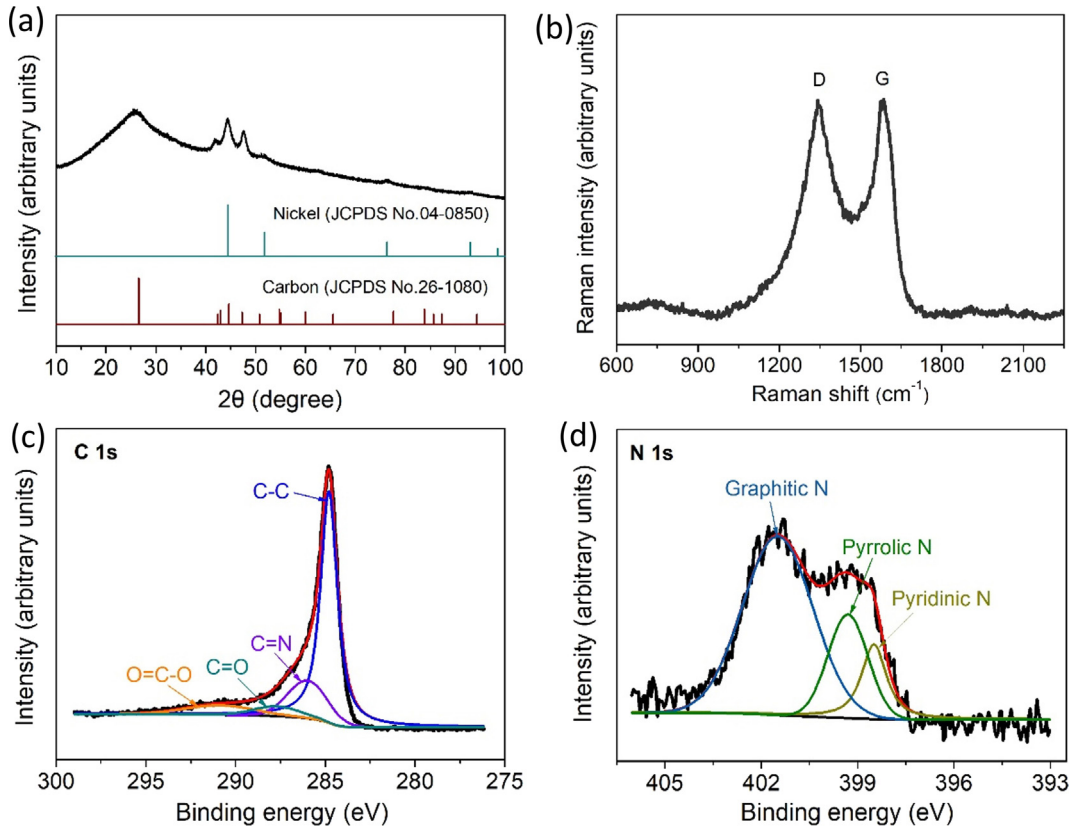

Fig. 3. (a) XRD pattern, (b) Raman spectrum, (c) C 1s XPS spectrum and (d) N 1s XPS spectrum of N-HCNs.

as-synthesized N-HCNs material is indeed very effective for anchoring platinum.

The HER electrocatalytic activity was assessed in a typical three-electrode cell setup in 0.5 M H_2SO_4 aqueous solution on a glassy-carbon electrode (GCE) with a mass loading of about 0.283 mg cm^{-2}. All tests were performed without iR compensation. During the *in-situ* Pt deposition process, the HER performance of N-HCNs continuously improved until it reached a stable state after 8000 CV cycles (Fig. 5a and d). The lineal sweep voltammetry (LSV) curves of N-HCNs and Pt@N-HCNs are present in Fig. 5b along with the commercial 5% Pt/C. As expected, Pt/C exhibits excellent HER performance. The N-HCNs requires overpotential (η) of 517 mV to reach current density (j) of 10 mA cm^{-2}, while the Pt@N-HCNs, in contrast, can provide j of 10 mA cm^{-2} and 20 mA cm^{-2} at η of about 30 and 60 mV, respectively. The Pt@N-HCNs shows excellent HER catalytic activity with negligible over potential, while the N-HCNs is poor HER catalyst, indicating that

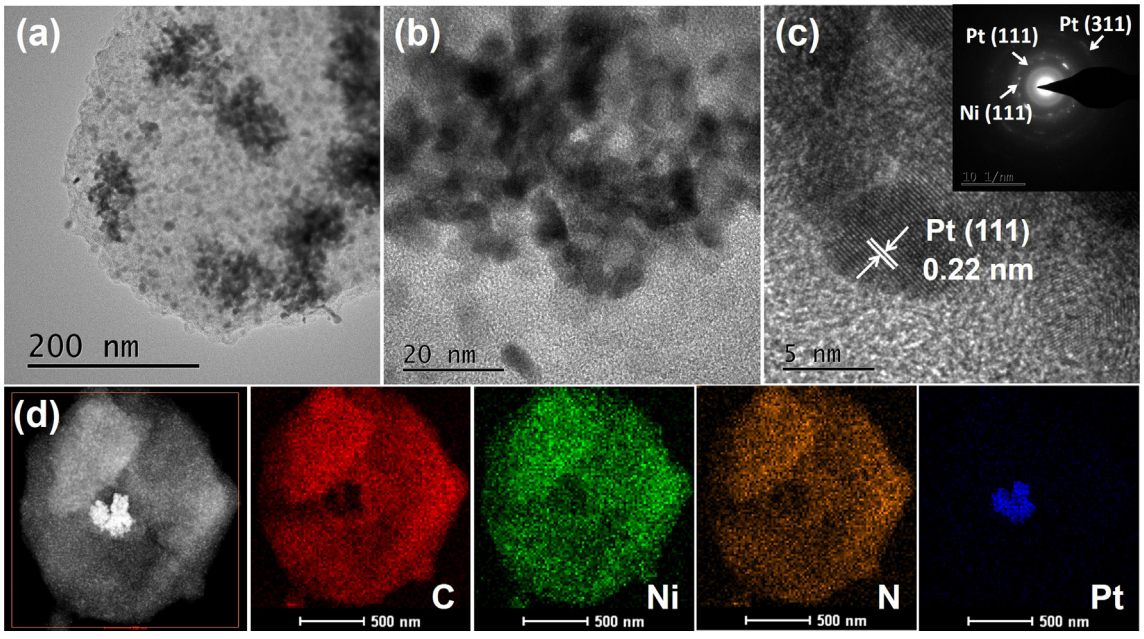

Fig. 4. (a) and (b) TEM images, (c) HRTEM image (inset: selected area electron diffraction pattern) and (d) elemental mappings of Pt@N-HCNs.

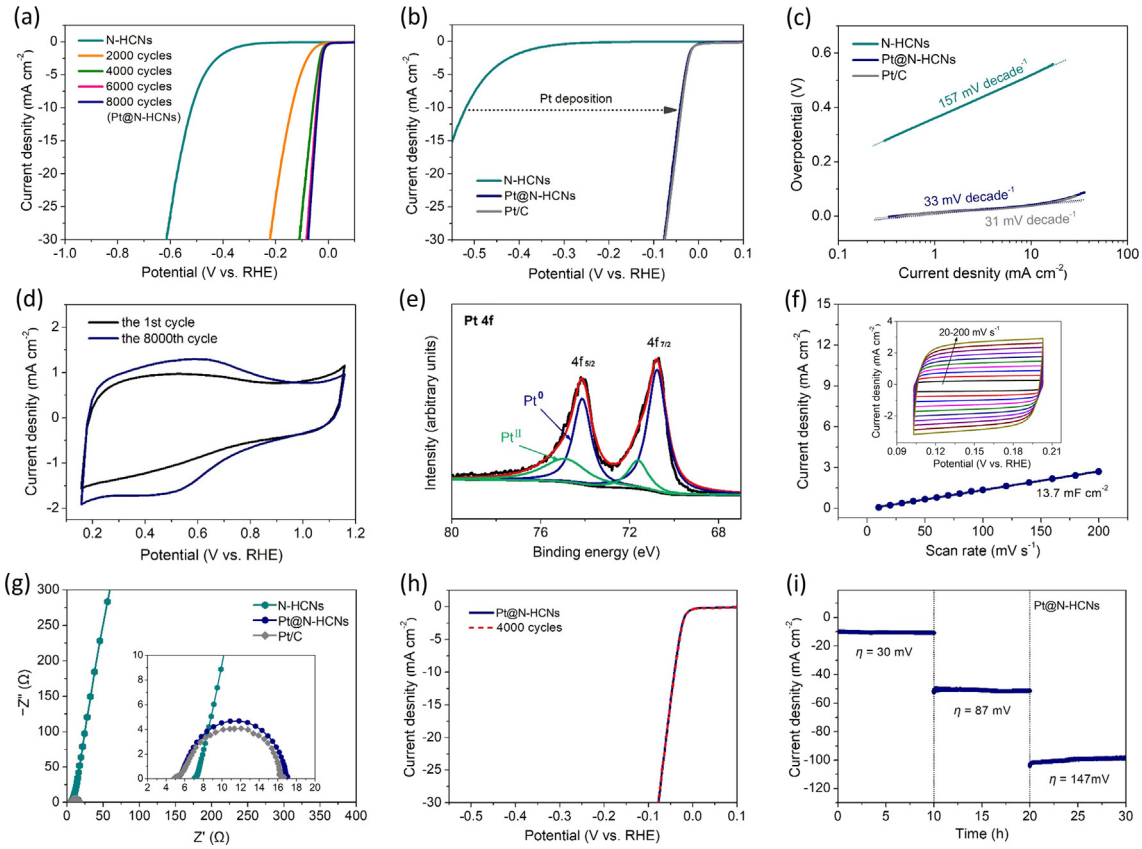

Fig. 5. (a) LSV curves of N-HCNs in the Pt deposition process after different CV cycles; (b) LSV curves and (c) Tafel plots of N-HCNs, Pt@N-HCNs and Pt/C, respectively; (d) CV curves of N-HCNs in the Pt deposition process for the 1st cycle and the 8000th cycle; (e) Pt 4f XPS spectrum of Pt@N-HCNs; (f) double-layer capacitance of Pt@N-HCNs (inset: CVs at scan rates from 20 to 200 mV s^{-1} in the potential range without redox current peaks); (g) Nyquist plots of N-HCNs, Pt@N-HCNs and Pt/C, respectively; (h) LSV curves of Pt@N-HCNs before and after 4000 CV cycles and (i) time-dependent current densities of Pt@N-HCNs under static overpotentials of 30, 87 and 147 mV respectively for total 30 h.

this huge improvement of performance is actually caused by Pt deposition.

Detailed underlying mechanism of HER activity was studied by Tafel plots acquired based on the LSV curves (Fig. 5c). The linear regions of Tafel plots are fitted to the Tafel equation (η = b log j + a, where b is the Tafel slope), yielding Tafel slopes of 157, 33 and 31 mV $decade^{-1}$ for N-HCNs, Pt@N-HCNs and Pt/C, respectively. The value for Pt/C catalyst is in agreement with the results of previous studies. The small Tafel slope of Pt@N-HCNs indicates that it follows the Volmer–Heyrovsky pathway as the electrochemical desorption is the rate-limiting step [54]. Charge storage capability of the N-HCNs and Pt@N-HCNs electrocatalysts was used to evaluate their electrochemically active surface areas. CV loops were recorded at scan rates from 20 to 200 mV s^{-1} in the potential range without redox current peaks (Figs. 5f and S5). The corresponding capacitance of 8.9 and 13.7 mF cm^{-2} for N-HCNs and Pt@N-HCNs respectively demonstrates that Pt@N-HCNs possesses a higher double-layer capacitance, which represents a larger active surface area. Electrochemical impedance spectroscopy (EIS) measurements were also performed to further investigate the interface reactions and electrode kinetics of the catalysts during HER process. The Nyquist plots of the N-HCNs, Pt@N-HCNs and Pt/C recorded at −22 mV vs. RHE are given in Fig. 5g. It shows similar small charge-transfer resistance of Pt@N-HCNs with Pt/C, suggesting faster electron transfer between the catalytic active sites and the electrode substrate, which is one of the key factors contributing to its superior HER kinetics.

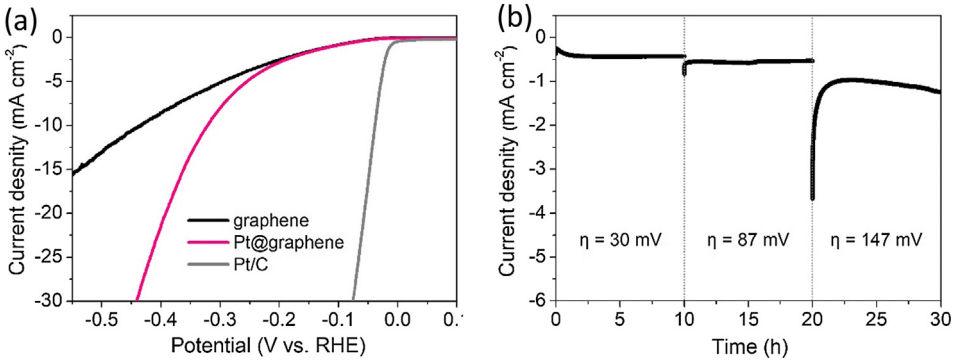

Fig. 6. (a) LSV of graphene, Pt@graphene and Pt/C and (b) time-dependent current densities of Pt@graphene under static overpotentials of 30, 87 and 147 mV for 10 h, respectively.

Durability is another pivotal concern for evaluating all the catalysts. In this study, LSV curve after 4000 CV cycles sweeping between +0.905 mV and −0.095 mV at 100 mV s^{-1} was also recorded for Pt@N-HCNs (Fig. 5h). As shown, the HER performance remains unchanged, indicating that Pt@N-HCNs exhibits prominent durability to withstand accelerated degradation. To further probe its durability in constant HER processes, chronoamperometry at overpotentials of 30, 87 and 147 mV respectively was conducted continuously for a total of 30 h. The corresponding current density curves are shown in Fig. 5i. The current densities are observed to be levelled out around 10, 50 and 100 mA cm^{-2}, respectively, which is consistent with the LSV data. No obvious degradation was found in these chronoamperometric curves. The superior HER durability of Pt@N-HCNs can be attributed to the high adsorption ability of the Pt on the surface of N-HCNs decorated electrode during the *in-situ* electrochemical deposition, yielding solid contact between Pt and N-HCNs.

For comparison, commercial graphene was also tested to deposit Pt NPs using this electrochemical method (Pt@graphene). Unfortunately, there is no noteworthy enhancement in the HER performance (Fig. 6a), and its long-time durability is also unsatisfactory, especially at high current densities (Fig. 6b), which indicates that few Pt NPs might be deposited on the graphene decorated electrode. Graphene is not very suitable for Pt NPs deposition probably due to the lack of anchoring sites.

According to the above results, the as-synthesized N-HCNs nanomaterial is suggested to be ideal support for dispersing of Pt NPs to obtain electrocatalyst with superior HER performance. There are two main probable reasons for the high HER performance of Pt@N-HCNs: First, the nanosized and partially graphitized structure of N-HCNs provides good conductivity that can facilitate the electron transport. Second, the uniformly doping of nitrogen and induced defects in N-HCNs provide sufficient active sites for Pt deposition. The strong interaction and synergistic effect between Pt and N-HCNs are beneficial for improving the electrocatalytic activity and durability of the catalyst.

4. Conclusions

In summary, a N-rich MOF (JUC-150) is selected in this work as precursor to prepare N-HCNs for Pt NPs deposition. The doped N atoms play a key role in creating active sites for Pt deposition, which is realized through a simple electrochemical method. The corresponding Pt@N-HCNs exhibits low onset overpotential, small Tafel slope, high current density and prolonged stability and durability. The excellent HER performance and superior stability can be attributed to the facilitated electron transport and synergistic effect between Pt and N-HCNs. In this way, carbon-based N-rich materials derived from MOFs are promising supports for Pt deposition via a simple electrochemical method, which may provide a general method to ensure the facile synthesis of Pt-containing composites and pave an avenue to the further development of functional applications of MOF materials.

Acknowledgments

This work was supported by the National Natural Science Foundation of China (Grant Nos. 21571187, 21501198, 21601205, 51702366, 21571076, 21776314), Taishan Scholar Foundation (ts201511019), and the Fundamental Research Funds for the Central Universities (18CX02047A, 18CX07001A, 18CX05018A, 15CX05012A).

References

[1] J.A. Turner, Science 285 (1999) 687–689.
[2] M.S. Dresselhaus, I.L. Thomas, Nature 414 (2001) 332–337.
[3] M.Z. Jacobson, W.G. Colella, D.M. Golden, Science 308 (2005) 1901–1905.
[4] D. Voiry, H. Yamaguchi, J. Li, R. Silva, D.C.B. Alves, T. Fujita, M. Chen, T. Asefa, V.B. Shenoy, G. Eda, M. Chhowalla, Nat. Mater. 12 (2013) 850–855.
[5] J.K. Nørskov, T. Bligaard, A. Logadottir, J.R. Kitchin, J.G. Chen, S. Pandelov, U. Stimming, J. Electrochem. Soc. 152 (2005) 23–26.
[6] M.G. Walter, E.L. Warren, J.R. McKone, S.W. Boettcher, Q. Mi, E.A. Santori, N.S. Lewis, Chem. Rev. 110 (2010) 6446–6473.
[7] F. Yang, Y. Zhao, Y. Du, Y. Chen, G. Cheng, S. Chen, W. Luo, Adv. Energy Mater. 8 (2018) 1703489.
[8] Y.G. Li, H.L. Wang, L.M. Xie, Y.Y. Liang, G.S. Hong, H.J. Dai, J. Am. Chem. Soc. 133 (2011) 7296–7299.
[9] H.T. Wang, Z.Y. Lu, S.C. Xu, D.S. Kong, J.J. Cha, G.Y. Zheng, P.C. Hsu, K. Yan, D. Bradshaw, F.B. Prinz, Y. Cui, Proc. Natl. Acad. Sci. USA 110 (2013) 19701–19706.
[10] S. Cobo, J. Heidkamp, P.-A. Jacques, J. Fize, V. Fourmond, L. Guetaz, B. Jousselme, V. Ivanova, H. Dau, S. Palacin, M. Fontecave, V. Artero, Nat. Mater. 11 (2012) 802–807.
[11] K.A. Kuttiyiel, K. Sasaki, W.-F. Chen, D. Su, R.R. Adzic, J. Mater. Chem. A 2 (2014) 591–594.
[12] H. Lin, Z. Shi, S. He, X. Yu, S. Wang, Q. Gao, Y. Tang, Chem. Sci. 7 (2016) 3399–3405.
[13] H. Vrubel, X. Hu, Angew. Chem. Int. Ed. 51 (2012) 12703–12706.
[14] E.J. Popczun, J.R. McKone, C.G. Read, A.J. Biacchi, A.M. Wiltrout, N.S. Lewis, R.E. Schaak, J. Am. Chem. Soc. 135 (2013) 9267–9270.
[15] C. Tang, R. Zhang, W. Lu, L. He, X. Jiang, A.M. Asiri, X. Sun, Adv. Mater. 29 (2017) 1602441.
[16] C. Du, L. Yang, F. Yang, G. Cheng, W. Luo, ACS Catal. 7 (2017) 4131–4137.
[17] D.-Y. Wang, M. Gong, H.-L. Chou, C.-J. Pan, H.-A. Chen, Y. Wu, M.-C. Lin, M. Guan, J. Yang, C.-W. Chen, Y.-L. Wang, B.-J. Hwang, C.-C. Chen, H. Dai, J. Am. Chem. Soc. 137 (2015) 1587–1592.
[18] D. Deng, L. Yu, X. Chen, G. Wang, L. Jin, X. Pan, J. Deng, G. Sun, X. Bao, Angew. Chem. Int. Ed. 52 (2013) 371–375.
[19] W. Zhou, J. Jia, J. Lu, L. Yang, D. Hou, G. Li, S. Chen, Nano Energy 28 (2016) 29–43.
[20] G.-R. Xu, J. Bai, J.-X. Jiang, J.-M. Lee, Y. Chen, Chem. Sci. 8 (2017) 8411–8418.
[21] X. Cheng, Y. Li, L. Zheng, Y. Yan, Y. Zhang, G. Chen, S. Sun, J. Zhang, Energy Environ. Sci. 10 (2017) 2450–2458.
[22] J. Ying, G. Jiang, Z. Paul Cano, L. Han, X.-Y. Yang, Z. Chen, Nano Energy 40 (2017) 88–94.
[23] T. Liu, F. Yang, G. Cheng, W. Luo, Small 14 (2018) 1703748.
[24] R. Liu, S.M. Mahurin, C. Li, R.R. Unocic, J.C. Idrobo, H. Gao, S.J. Pennycook, S. Dai, Angew. Chem. Int. Ed. 50 (2011) 6799–6802.
[25] C. Galeano, C. Baldizzone, H. Bongard, B. Spliethoff, C. Weidenthaler, J.C. Meier, K.J. Mayrhofer, F. Schüth, Adv. Funct. Mater. 24 (2014) 220–232.
[26] G.-H. Wang, J. Hilgert, F.H. Richter, F. Wang, H.-J. Bongard, B. Spliethoff, C. Weidenthaler, F. Schüth, Nat. Mater. 13 (2014) 293–300.
[27] L. Ji, J. Wang, S. Zuo, Z. Chen, J. Phys. Chem. C 121 (2017) 8923–8930.
[28] Z. Ju, S. Yan, D. Yuan, Chem. Mater. 28 (2016) 2000–2010.
[29] A. Cadiau, Y. Belmabkhout, K. Adil, P.M. Bhatt, R.S. Pillai, A. Shkurenko, C. Martineau-Corcos, G. Maurin, M. Eddaoudi, Science 356 (2017) 731–735.
[30] K. Shen, L. Zhang, X. Chen, L. Liu, D. Zhang, Y. Han, J. Chen, J. Long, R. Luque, Y. Li, B. Chen, Science 359 (2018) 206–210.
[31] P.-Q. Liao, N.-Y. Huang, W.-X. Zhang, J.-P. Zhang, X.-M. Chen, Science 356 (2017) 1193–1196.
[32] L. Liang, C. Liu, F. Jiang, Q. Chen, L. Zhang, H. Xue, H.-L. Jiang, J. Qian, D. Yuan, M. Hong, Nat. Commun. 8 (2017) 1233.
[33] Y.H. Qian, T. An, K.E. Birgersson, Z.L. Liu, D. Zhao, Small 14 (2018) 1704169.
[34] H.-L. Jiang, B. Liu, Y.-Q. Lan, K. Kuratani, T. Akita, H. Shioyama, F. Zong, Q. Xu, J. Am. Chem. Soc. 133 (2011) (1857) 11854–11861.
[35] H.-S. Lu, H. Zhang, R. Liu, X. Zhang, H. Zhao, G. Wang, Appl. Surf. Sci. 392 (2017) 402–409.
[36] S. Mandegarzad, J.B. Raoof, S.R. Hosseini, R. Ojani, Appl. Surf. Sci. 436 (2018) 451–459.
[37] S. Pandiaraj, H.B. Aiyappa, R. Banerjee, S. Kurungot, Chem. Commun. 50 (2014) 3363–3366.
[38] F. Yang, Y. Chen, G. Cheng, S. Chen, W. Luo, ACS Catal. 7 (2017) 3824–3831.
[39] J. He, W. Lv, Y. Chen, J. Xiong, K. Wen, C. Xu, W. Zhang, Y. Li, W. Qin, W. He, J. Mater. Chem. A 6 (2018) 10466–10473.
[40] J. He, W. Lv, Y. Chen, J. Xiong, K. Wen, C. Xu, W. Zhang, Y. Li, W. Qin, W. He, J. Power Sources 363 (2017) 103–109.
[41] G. Srinivas, V. Krungleviciute, Z.-X. Guo, T. Yildirim, Energy Environ. Sci. 7 (2014) 335–342.
[42] R.R. Salunkhe, Y.V. Kaneti, J. Kim, J.H. Kim, Y. Yamauchi, Acc. Chem. Res. 49 (2016) 2796–2806.
[43] L. Yan, L. Cao, P. Dai, X. Gu, D. Liu, L. Li, Y. Wang, X. Zhao, Adv. Funct. Mater. 27 (2017) 1703455.
[44] Z. Li, C. Li, X. Ge, J. Ma, Z. Zhang, Q. Li, C. Wang, L. Yin, Nano Energy 23 (2016) 15–26.
[45] J. He, Y. Chen, W. Lv, K. Wen, C. Xu, W. Zhang, Y. Li, W. Qin, W. He, ACS Nano 10 (2016) 10981–10987.
[46] J. He, W. Lv, Y. Chen, K. Wen, C. Xu, W. Zhang, Y. Li, W. Qin, W. He, ACS Nano 11 (2017) 8144–8152.
[47] J. He, Y. Chen, A. Manthiram, Energy Environ. Sci. (2018), https://doi.org/10.1039/C8EE00893K.
[48] K. Shen, X. Chen, J. Chen, Y. Li, ACS Catal. 6 (2016) 5887–5903.
[49] L. Yang, X. Zeng, W. Wang, D. Cao, Adv. Funct. Mater. 28 (2018) 1704537.
[50] Y. Qian, I.A. Khan, D. Zhao, Small 13 (2017) 1701143.
[51] X. Zeng, J. Shui, X. Liu, Q. Liu, Y. Li, J. Shang, L. Zheng, R. Yu, Adv. Energy Mater. 8 (2018) 1701345.
[52] J. Zhang, P. Liu, G. Wang, P.P. Zhang, X.D. Zhuang, M.W. Chen, I.M. Weidinger, X.L. Feng, J. Mater. Chem. A 5 (2017) 25314–25318.
[53] Z. Kang, M. Xue, L. Fan, L. Huang, L. Guo, G. Wei, B. Chen, S. Qiu, Energy Environ. Sci. 7 (2014) 4053–4060.
[54] B.E. Conway, B.V. Tilak, Electrochim. Acta 47 (2002) 3571–3594.